

1 **Comparison of aerosol optical depth from satellite (MODIS),**
2 **sun photometer and broadband pyrliometer ground-based**
3 **observations in Cuba.**
4

5 Juan Carlos Antuña-Marrero¹, Victoria Cachorro Revilla², Frank García Parrado¹, Ángel de
6 Frutos Baraja², Albeth Rodríguez Vega¹, David Mateos², René Estevan Arredondo^{3,1}, Carlos
7 Toledano²

8
9 ¹ Atmospheric Optics Group of Camagüey (GOAC), Meteorological Institute of Cuba, Camagüey, Cuba

10 ² Atmospheric Optics Group (GOA), University of Valladolid (UVA), Valladolid, Spain

11 ³ Huancayo Observatory, Geophysical Institute of Peru, Huancayo, Peru
12
13
14
15
16
17

18 Resubmitted to *Atmospheric Measurement Techniques*

19
20 March 2018
21
22
23
24

25 Corresponding author:

26 Juan Carlos Antuña-Marrero

27 Atmospheric Optics Group of Camagüey

28 Meteorological Institute of Cuba

29 Camagüey, Cuba

30 Email: jcam45@gmail.com
31
32

33 **Abstract**

34 In the present study, we report the first comparison between the aerosol optical depth
35 (AOD) and Angstrom exponent (AE) of the MODerate resolution Imaging Spectroradiometer
36 (MODIS) instruments on the Terra (AOD_t) and Aqua (AOD_a) satellites and those measured using
37 a sun photometer (AOD_{SP}) at Camagüey, Cuba, for the period 2008 to 2014. The comparison of
38 Terra and Aqua data includes AOD derived with both Deep Blue (DB) and Dark Target (DT)
39 algorithms from MODIS Collection 6. Combined Terra and Aqua (AOD_{ta}) data were also
40 considered. Assuming an interval of ± 30 minutes around the overpass **time** and the area of 25 km
41 around the sun photometer **site**, two **coincidence** criteria were **considered**: individual pairs of
42 observations, and both spatial and temporal mean values, which we call collocated daily means.
43 The usual statistics (BIAS, MAE, RMSE) together with linear regression analysis are used for this
44 comparison. Results show very similar values for both **coincidence** criteria: DT algorithm
45 generally displays **better** statistics and higher homogeneity than the DB algorithm **in the**
46 **behaviour of AOD_t, AOD_a, AOD_{ta} as compared to AOD_{SP}. For collocated daily means: a)**
47 mean square errors (RMSE) of 0.060 and 0.062 were obtained for Terra and Aqua with the DT
48 algorithm and 0.084 and 0.065 for the DB algorithm; **b) MAE follows the same patterns; c) BIAS**
49 **for both Terra and Aqua presents positive and negative values but its absolute values are lower**
50 **for the DT algorithm; d) Combined AOD_{ta} data also give lower values of these three statistical**
51 **indicators for the DT algorithm; e) both** algorithms present good correlations for comparing
52 AOD_t, AOD_a, AOD_{ta} vs. AOD_{SP}, **with a slight overestimation of satellite data compared to**
53 **AOD_{SP}, f) DT algorithm yields better figures with slopes of 0.96 (Terra), 0.96 (Aqua) and 0.96**
54 **(Terra+Aqua) compared to the DB algorithm (1.07, 0.90, 0.99) that displays greater variability.**
55 **Multiannual monthly means of AOD_{ta} establish a first climatology more comparable to that**

56 **given by the sun-photometer and their statistical evaluation reveals better agreement** with
57 **AOD_{SP} for the DT algorithm. Results of the AE comparison** showed similar results to those
58 reported in the literature concerning the two algorithms' capacity for retrieval. A comparison
59 between broadband **optical depths (BAOD), derived** from broadband pyrheliometer observations
60 at the Camagüey site and three other meteorological stations in Cuba, and AOD observations from
61 MODIS on board Terra and Aqua show a poor correlation with slopes below 0.4 for both
62 algorithms. Aqua (Terra) showed RMSE values of 0.073(0.080) and 0.088(0.087) for the DB and
63 DT algorithms. As expected, RMSE values are higher than those from the MODIS/sun photometer
64 comparison, **but within** the same order of magnitude. Results from the BAOD, derived from solar
65 radiation measurements, demonstrate its reliability to describe **climatological** AOD series
66 estimates.

67

68 KEY WORDS: atmosphere, remote sensing, aerosols, Aerosol Optical Depth (AOD), Broadband
69 Aerosol optical depth (BAOD), AERONET, MODIS

70

71 **1. Introduction**

72 Atmospheric aerosols play an important role in weather and climate (IPPC 2013). Depending on
73 the physical/chemical and optical properties of atmospheric aerosols together with their origin and
74 spatial and temporal distribution, they can affect the Earth's radiative budget, as well as dynamic,
75 biogeochemical and chemical processes (Knippertz and Stuut, 2014; Seinfeld and Pandis, 2016).
76 All of these processes play a key role at a global and regional scale due to the high spatio-temporal
77 variability of aerosol properties. Aerosols can also affect the biosphere and, in particular, humans
78 in several ways: for example, the Saharan dust transported to America across the Atlantic supplies

79 nutrients to the Amazon forest (Swap et al., 1992; Yu et al., 2015). Moreover, in the Caribbean, in
80 addition to aerosols of local origin, dust makes the amount of aerosol exceed air quality standards
81 associated to human health (Prospero and Lamb, 2003; Prospero et al., 2014). The great variability
82 of Saharan dust transported to the Caribbean basin has been documented using long-term
83 observations in Barbados (Prospero and Lamb, 2003; Prospero and Mayol-Bracero, 2013) and
84 more recently in Miami, Guadeloupe and Cayenne (Prospero et al., 2014). The Caribbean region
85 is thus of great importance for aerosol studies due to its low aerosol background, which helps
86 aerosol transport studies (Kaufman et al., 2005; Denjean et al., 2016; Velasco et al., 2018). One
87 difficulty, however, is that it is an area where land and water make up a mixed pixel when remote
88 satellite aerosol studies are carried out.

89 In order to improve calculations of aerosol climatology for Cuban land areas, which
90 remains ongoing, we compared aerosol ground-based observations and available satellite data, as
91 a first step towards assessing this climatology. This involves a comparison between all the
92 available Camagüey sun photometer aerosol optical depth (AOD) data and the BAOD provided
93 by solar radiation measurements with the series of AOD (550 nm) from the MODerate resolution
94 Imaging Spectroradiometer (MODIS) instruments on board the Terra (2001 to 2015) and Aqua
95 (2002 to 2015) satellites. Selected observations were those spatially and temporally collocated
96 between satellite instruments and ground-based sites. In addition to the aerosol load given by the
97 AOD, we also evaluated the Ångström exponent (AE) as a parameter providing information about
98 particle size for MODIS and sun photometer data.

99 One of the challenges we faced was the low amount of potential coincident AOD and AE
100 from MODIS and the Sun photometer. The same is true for AOD from MODIS and broadband
101 pyrliometer derived BAOD, in both cases due to existing gaps in the ground-based time series

102 and also because this area is strongly affected by clouds (mainly partially cloud cover). In order to
103 maximize the number of satellite and surface measurement pairs, we used primary AOD and AE
104 L2 products without any averaging as well as combined AOD and AE from Terra and Aqua
105 MODIS sensors as a whole dataset. We also used Deep Blue (DB) and Dark Target (DT)
106 algorithms to evaluate the reliability of satellite AOD and AE retrievals to select the most
107 appropriate data set to derive the climatology of both AOD/AE aerosol parameters in Cuba.

108 The earliest attempt to measure aerosol optical properties at ground level in Cuba recorded
109 in a scientific publication dates back to 1988 (Martinez, 1988) where the Linke turbidity factor
110 and the Ångström β turbidity coefficient were derived from solar direct normal irradiance (DNI)
111 measurements. Twenty years later, a cooperation agreement between scientific institutions in
112 Spain and Cuba enabled a Cimel CE-318 sun photometer to be installed at Camagüey (Cuba) and
113 for it to be included in the Aerosol Robotic Network (AERONET, Holben et al., 1998). Several
114 aerosol studies have been conducted using the Aerosol Optical Depth (AOD) and AE from
115 Camagüey's sun photometer observations (see, Antuña-Marrero et al., 2016;
116 <http://www.goac.cu/uva/>).

117 Broadband pyrheliometric DNI observations allow the Broadband Aerosol Optical Depth
118 (BAOD) to be determined, which complements sun photometer aerosol observations at Camagüey,
119 and provides aerosol information at three other locations in Cuba. The main purpose of
120 determining BAOD is to offer information concerning aerosol variability over the island, also
121 making it possible to extend aerosol records back in time. The first BAOD calculations used for
122 DNI measurement were conducted at Camagüey under clear sky conditions for the period 1985-
123 2007 using Gueymard's (1998) improved parameterizations (Fonte and Antuña, 2011). García et
124 al. (2015) used this kind of DNI observation for a longer period (1981-2013) and compared this

125 BAOD to sun-photometer AOD data. They used observations under the clear line of sight between
126 the broadband pyrheliometer and a region of 5° around the Sun, as well as improved climatological
127 values of the integrated water vapor.

128 This comparative analysis does not aim to be a validation study of the MODIS sensor since
129 many works during the long history of the MODIS sensor on the Terra and Aqua platforms have
130 sought to improve its features (these include: Kaufman et al., 1997a, b; Tanré et al., 1997; Remer
131 et al., 2002, 2005, 2006; Hsu, et al., 2004,2006, 2013; Levy et al., 2007; 2009; 2010, 2013, 2015;
132 Sayer et al., 2013, 2014; <https://darktarget.gsfc.nasa.gov/atbd/overview>). However, compared to
133 other areas of the world, no studies have been reported in the Caribbean region and in Cuba in
134 particular (Papadimas et al., 2009; Mishchenko, et al., 2010; Kahn et al., 2011; Bennouna et al.,
135 2011, 2013; Witte et al., 2011; Gkikas et al., 2013; 2015; Levy et al., 2015).

136 As mentioned, our aim is to establish reliable aerosol climatology in Cuba based on satellite
137 and ground-based instruments. By making a detailed comparison of similarities and differences
138 between available data sets, the present work seeks to make a contribution to said aim.

139 The article is structured as follows. Section 2 begins with the description of the datasets,
140 followed by the explanation of the coincidence criteria between the AOD and AE MODIS L2
141 products and the same two variables from the sun photometer and broadband pyrheliometer
142 BAOD. This section ends with the explanation of the statistical indices used. Section 3 is composed
143 of various sections designed to explain and discuss the large volume of results to emerge from the
144 comparison given by taking two different retrieval AOD aerosol algorithms, for both the Terra and
145 Aqua platforms, with the sun photometer and BAOD. Section 4 contains a summary of the
146 conclusions.

147

148 **2. Materials and Methods**

149 **2.1 MODIS satellite instruments**

150 The twin MODIS instruments on board the Terra and Aqua satellites have accumulated
151 over 15 years of observations of several atmospheric parameters, including AOD at several
152 wavelengths and the AE parameter, the two most common parameters for describing atmospheric
153 aerosol optical properties. Based on the assumptions about the properties of the Earth's surface
154 and the aerosol type expected over these surfaces, the MODIS Atmosphere team developed three
155 algorithms for processing MODIS observations (Levy et al., 2013). Regions which appear visually
156 "dark" from space, referred to as Dark Target (DT), include the algorithm assumptions for
157 vegetated land surfaces (Kaufman et al., 1997a, b) and for remote ocean regions (Tanré et al.,
158 1997). The third algorithm, called the Deep Blue (DB) algorithm, includes assumptions for
159 surfaces which are visually "bright" from space and uses near-UV wavelengths (DB band near 410
160 nm). Under these conditions, the DB band provides a better signal than the visible wavelengths,
161 improving the information content for aerosol retrievals (Hsu et al., 2004; 2006) due to lower
162 surface albedo at this short wavelength. Levy et al. (2013) provide a detailed explanation of basic
163 MODIS retrieval concepts and improvements to the DT algorithm in Collection 6 for aerosol
164 products. In addition, Hsu et al. (2013) give a detailed explanation of the DB algorithm
165 improvements in Collection 6.

166 Following Levy et al. (2013), we summarize the MODIS calculus chain. MODIS Level 0
167 (L0) is the basic data file containing raw observations from the sensors. Observations grouped in
168 five-minute swath scans (called granules) are Level 1A (L1A), which after calibration becomes
169 Level 1B (L1B). L1B data feed the MODIS geophysical retrieval algorithms, generating the
170 primary geophysical observations, which include AOD and AE, designated Level 2 (L2). This is

171 followed by Level 3 (L3), consisting of daily and monthly statistics of geophysical products, in 1°
172 $\times 1^\circ$ latitude\longitude grid boxes. L2 aerosol products are stored in the MOD04 (Terra) and
173 MYD04 (Aqua) files.

174 We selected AOD at 550 nm from MODIS (both on Terra and Aqua satellites) Collection
175 6, L2 data level derived using the two algorithms; DB for land with the highest data quality
176 (Quality flag = 2, 3) and DT for land, corrected (Quality flag = 3). In addition, we selected the AE
177 retrieved over land from the DB algorithm using the corresponding pairs of AOD values (412/470
178 nm or 470/650 nm) with the highest quality (Quality flag = 2, 3), since the DT algorithm only
179 retrieves the AE over the ocean (Table B1 in Levy et al., 2013). Table 1 lists the aerosol products
180 used in the present study.

181 At a global scale, it has been established that using the DT algorithm over land, MODIS-
182 retrieved aerosol size parameters evidence poor quantitative capacity, particularly AE (e.g., Levy
183 et al., 2010; Mielonen et al., 2011). However, for the DB algorithm, AE capacity increases for
184 moderate or high aerosol loadings, $AOD > 0.3$ (Sayer et al., 2013). We therefore decided to
185 conduct the comparison between the AE from the MODIS DB algorithm and the AE from the
186 Camagüey sun photometer to estimate its uncertainty. The enhanced DB algorithm methodology
187 for deriving AE in Collection 6 is the same as in Collection 5. It uses the Ångström power law and
188 AOD values at 412, 470 and 650 nm. Under non-vegetated surfaces, AE is derived using the AOD
189 from pair 412/470 nm. For vegetated surfaces, AE is derived from the 470/650 nm pair. In the case
190 of a surface with mixed vegetated and non-vegetated areas, AE is derived using the AOD at the
191 three wavelengths mentioned (Hsu et al., 2013).

192

193

194 **2.2 Camagüey AERONET sun-photometer**

195 The Camagüey sun photometer, installed thanks to an agreement between the University
196 of Valladolid (UVA), Spain, and the Meteorological Institute of Cuba (INSMET) for joint aerosol
197 research, contributes to the NASA Aerosol Robotic Network (AERONET) (Antuña et al., 2012).
198 Annual replacement of the instrument for one calibrated, sent from Valladolid to Camagüey,
199 encountered numerous transportation and customs delays, causing gaps in the observation series.
200 However, the collected series of observations does represent a valuable dataset of aerosol columnar
201 optical properties in the Caribbean, enabling GOAC-INSMET and GOA-UVA to conduct
202 preliminary aerosol research (Antuña-Marrero et al, 2016).

203 The AERONET Cimel sun photometers have been conducting aerosol observations at nine
204 spectral narrow band filters for over two decades, producing spectral AOD and column effective
205 particle properties (Holben et al., 1998). In general, Cimel sun photometer nominal wavelengths
206 are 340, 380, 440, 500, 675, 870, 935, 1020 and 1640 nm. In some cases, the 1640 nm is replaced
207 by a 1240 nm. Its processing algorithm, based on the Beer-Lambert-Bouguer law, allows spectral
208 OD values at an uncertainty level of approximately 0.01 to 0.02 to be determined (Holben et al.,
209 1998; Eck et al., 1999). Because of this low level of uncertainty, AERONET AOD observations
210 commonly serve as reference values (“ground truth”) to validate AOD measured by other remote
211 sensing sensors (Zhao et al., 2002). AERONET AE are derived for five different wavelength
212 intervals; 340-440 nm, 380-500 nm, 440-675 nm, 440-870 nm and 500-870 nm. In the present
213 study, the selected AE is the one in the 440-675 nm range (AE_{SP}).

214 We used Camagüey sun photometer Level 2.0 data as processed by AERONET, i.e., cloud
215 screened and quality-assured (Smirnov et al., 2000), covering the period from 7 October 2008 to
216 1 August 2014. This consisted of 29,940 single AOD (340 to 1640nm) and AE_{SP} observations.

217 Applying the Ångström power law, we converted single sun photometer AOD observations at 500
218 nm wavelength to AOD at 550nm, (AOD_{SP}) using the AE_{SP} from the same measurement:

219

$$AOD_{SP} = AOD_{500} \left(\frac{\lambda_{550}}{\lambda_{500}} \right)^{-AE_{SP}} \quad (1)$$

220

221 ***2.3 Solar direct irradiance measurements and derived Broadband Aerosol Optical*** 222 ***Depth(BAOD)***

223 Four actinometrical stations belonging to the “Diagnostic Service for Solar Radiation in Cuba”
224 provided the DNI observations used to derive the BAOD (Antuña et al., 2008; 2011). Table 2 lists
225 the WMO code of the four stations, the geographical location and the number of observations
226 available for the periods at each station. Figure 1 shows the geographical location of the four
227 stations. The stations are equipped with Yanishevsky manual broadband solar radiation
228 instruments supplied between the 1970s and 1980s by the Hydrometeorological Service of the
229 Soviet Union. The Yanishevski broadband pyrheliometer is the M-3 model, a thermo-battery
230 system with a 5° field of view connected to an analogic galvanometer, GSA-1MA or GSA-1MB
231 model (GGO, 1957).

232 Calibrations of all the actinometrical instruments are conducted periodically by comparison
233 with a master broadband pyrheliometer and a master pyranometer. Trained observers perform
234 hourly manual observations from sunset to sunrise, following the standard methodologies and
235 quality control procedures established for this set of instruments (GGO, 1957). Once manual
236 measurement is conducted and recorded in a notebook designed for the purpose, all the
237 measurement information is digitized using Actino version 2.0 software (Estevan, 2010; Antuña
238 et al., 2008) of the “Diagnostic Service of the Broadband Aerosol & Clouds Optical Depth for

239 Cuba” (<http://www.goac.cu/eoc/>), a public service provided by GOAC. The software includes a
240 robust quality control of input data, its processing and output quality control (Antuña et al., 2011).
241 Because of the ageing of the Soviet era instruments, the magnitude of the error associated to the
242 broadband pyrheliometers currently operating in Cuba is estimated to be around 10 %.

243 Based on the model parameterization of solar broadband irradiances, the integrated aerosol
244 optical depth δ_a , BAOD, can be obtained using equation (2), where direct normal solar irradiance
245 (DNI) is measured and the remaining variables are determined independently (Gueymard, 1998).

246

$$247 \quad \delta_a = \left(\frac{1}{m_a} \right) \left[\ln \left(\frac{E_{0n}}{DNI} \right) - m_R \delta_c - m_w \delta_w - m_{nt} \delta_{nt} \right] \quad (2)$$

248 The individual atmospheric processes considered are: Rayleigh scattering, absorption by
249 ozone (O₃), stratospheric and tropospheric nitrogen dioxide (NO₂), uniformly mixed gases, water
250 vapor, and extinction (mostly scattering) by aerosols. The variables in equation (2) are: optical air
251 mass of aerosols (m_a), Rayleigh scattering, uniformed mixed gases, O₃ absorption and
252 stratospheric NO₂ (m_R), water vapor (m_w) and tropospheric NO₂ (m_{nt}) and similarly the
253 corresponding broadband optical depths δ . The method makes a series of assumptions, i.e.,
254 Bouguer’s law; in the strict sense that it is only valid for monochromatic radiation and is applied
255 to define broadband transmittance. For a detailed description of the derivation of equation (2) and
256 the parameterization of the variables, see Gueymard, (1998), and Fonte and Antuña (2012) and
257 García et al. (2015) for the method’s application to our data.

258 In order to avoid cloud contamination in BAOD retrieval, we used only DNI observations
259 with the cloud-free condition in the line of sight to the sun, in other words with a clear line of sight
260 between the broadband pyrheliometer and a region of 5° around the sun (GOAC, 2010).
261 Furthermore, to avoid errors associated with high elevation zenith angles, causing larger air

262 masses, DNI observations performed at 6:00 and 18:00 Local Time (LT) were not used in the
263 present study.

264 The main errors of the method for determining BAOD are associated to instrumental errors
265 and the error when estimating the precipitable water (PW) component (Gueymard, 2013). In the
266 first case, in order to ensure the quality of the solar radiation dataset from the four actinometrical
267 stations used in this study, including DNI, they are regularly subject to a two-step quality control
268 (Estevan et al., 2012). The first step applies the standard procedures designed for Yanishevski type
269 actinometrical instruments from the former Soviet Hydro-Meteorological Service (Kirilov et al.,
270 1957). Data that pass this quality procedure are then evaluated following the standards set by the
271 Baseline Solar Radiation Network - BSRN (Ohmura 1998, Long and Shi, 2006; 2008; Estevan et
272 al., 2012).

273 The size of the field of view of the broadband pyrhemometers is another potential source
274 of error since, in certain cases, circumsolar radiation causes more radiation to be measured than
275 expected. In such cases, the effect is an underestimation of BAOD. Nevertheless, this effect is low
276 in general, except in specific conditions such as large air masses, in the presence of high aerosol
277 loads or of large-particle aerosols (Gueymard, 1998).

278 Monthly mean PW values at the four actinometrical stations were used as input to derive
279 monthly mean δ_w values (Gueymard, 1998). For Camagüey, we calculated the monthly mean PW
280 values from the sun photometer PW observations from 2008 to 2014 (García et al., 2015). For
281 each of the three other stations, we calculated the monthly mean PW values using the vertical
282 integrated water vapor (kg m^{-2}) from spatially coincident ERA-Interim reanalysis between 1979
283 and 2013 (Barja et al., 2015). Taking into account all the above-mentioned errors, the total
284 uncertainty of the method used to determine BAOD is in the order of 10^{-2} (Gueymard, 1998).

285 **2.4 Coincidence criteria for MODIS and Sun photometer observations**

286 Obtaining sufficient AOD satellite observations over land for climatological studies in
287 insular areas poses a challenge when compared to the amount of data usually available over
288 continental regions such as the US, Europe or China. The reason tends to be the small size of the
289 islands. In the case of Cuba, its particular narrow latitudinal and elongated longitudinal extension
290 combined with its irregular coasts renders the MODIS L3 product unsuitable for climatological
291 studies. As can be seen in Figure 1, most of the 1° by 1° grid cells consist of both land and sea
292 areas, resulting from the merging AOD measured over the two surfaces. The red grid cell in Figure
293 1 is an example of the limitations of MODIS L3 products to represent land areas in the case of
294 Cuba. In response to this, we plan to use the MODIS L2 product to produce aerosol climatology
295 for Cuba rather than L3, which is commonly used for this type of studies. In this regard, it is vital
296 to validate the single observations from MODIS L2 with the single sun photometer observations.
297 We designed and applied a method to maximize the available pairs of MODIS L2 and sun
298 photometer AOD and AE observations coincident in space and time, avoiding duplicating the use
299 of any of them. Additionally, in an effort to increase the amount of data, we tested the differences
300 between Terra and Aqua L2 MODIS AOD and AE observations in order to determine the possible
301 combination of both Terra and Aqua in a single dataset.

302 Hereinafter, AOD_t , AOD_a , AOD_{ta} and AOD_{SP} will denote spatio-temporal AOD from
303 collocated MODIS (Terra, Aqua and Terra + Aqua) and AERONET sun photometer data,
304 respectively. Unless otherwise indicated, “AOD” refers to AOD at 550 nm wavelength. Similarly,
305 AE from Terra, Aqua and Terra + Aqua derived using only the DB algorithm will be denoted as
306 AE_t , AE_a and AE_{ta} .

307 Given the challenges arising from the small amount of potential coincident spatial and
308 temporal AOD_t and AOD_a with AOD_{SP} and BAOD, as explained above, we used MODIS L2 data
309 to maximize the amount of available MODIS observations for comparison. Hereinafter, we call
310 these observations “single observation values”; using the same denomination for the instantaneous
311 sun photometer observations on each day and for hourly broadband pyrhelimeter observations.
312 Another way to increase the amount of data was to combine AOD_t and AOD_a (AOD_{ta}) for
313 comparison with AOD_{SP} and BAOD. In these cases, different observations of AOD_{SP} and BAOD
314 match AOD_t and AOD_a because the time difference established for coincidence (± 30 min) is lower
315 than the difference between the Terra and Aqua daily overpass times.

316 Spatial coincidence criteria were guaranteed by selecting all the AOD_t and AOD_a measured
317 inside the 25 km radius around the sun photometer site for the whole data period from each satellite
318 sensor. Table 3 shows the amount of spatial coincident information for non-negative AOD_t and
319 AOD_a values. It shows the amount of data available for the whole period 2001 to 2015, when
320 broadband pyrhelimeter observations at Camagüey are available, and 2008 to 2014, the period of
321 available sun photometer observations. There are at least twice as many available observations
322 from Terra as from Aqua for the two periods. The greater number of available data from Terra
323 compared to Aqua is associated to the different overpass times of the two satellites over Cuba.
324 Figure 2 shows that Terra overpasses occur in the mid to late morning before convective activity
325 begins, while the Aqua overpasses take place in the early afternoon when convection has already
326 begun, causing a higher number of observations to be discarded in AOD retrievals due to cloud
327 presence.

328 **2.4.1 Collocated “*Single observation*” values and “*daily mean*” values**

329 All Aqua and Terra overpass times in a radius of 25 km around Camagüey for the periods
330 2001 to 2015 (Terra) and 2002 to 2015 (Aqua) are shown in Figure 2. Overpass times, defined by
331 the maximum and minimum values of all the 25 km spatially coincident MODIS observations, are
332 10:12 – 11:49 (LT) for Terra and 12:47 – 14:20 (LT) for Aqua. In addition, Figure 2 shows the
333 diurnal frequency of sun photometer observations from 2008 to 2014, and the diurnal frequency
334 of the BAOD observations for Camagüey for the period 1981 to 2015. Note that the BAOD
335 histogram shows only hourly frequency values, since that is the time interval between the manual
336 pyrhelimetric observations.

337 For each day, we compared the corresponding time of each single sun photometer
338 measurement with the time of each single AOD_t and AOD_a observation located in a radius of 25
339 km around the sun photometer site (an area of almost 2,000 km²) and in the time window of ± 30
340 minutes between both types of observations. The former selection process includes, for each
341 satellite, the AOD_t and AOD_a values derived both with the DB and DT processing algorithms
342 separately, producing four independent bulk datasets, two for Aqua and two for Terra. We then
343 identified four different cases of matching data per day in the bulk coincident datasets. The first
344 consisted of days with only one AOD_{SP} value and one AOD_t (AOD_a) coincident value, and the
345 second, only one AOD_{SP} value coincident with multiple AOD_t (AOD_a) values each day. In the
346 third case, only one AOD_t (AOD_a) value coincided with multiple AOD_{SP} values. Finally, the fourth
347 case consisted of multiple AOD_{SP} values coincident with multiple AOD_t (AOD_a) values.

348 Coincident cases were then selected for comparison, case by case. In the first instance, we
349 selected all cases. In the second case, because of the MODIS instruments spatiotemporal sampling
350 geometry, time differences between MODIS and sun photometer observations are in the order of
351 one minute. As a result, only the criterion of the minimum distance between the positions of the

352 AOD_t (AOD_a) and the sun photometer was applied to determine the pair of coincident values,
353 therefore not allowing any repeated AOD_{SP} and AOD_t (AOD_a) values to be selected. Since it
354 consists of only one AOD_t (AOD_a) measurement and multiple AOD_{SP} observations, in the third
355 case the distance is the same; hence the selection criteria was the minimum of the time differences
356 between AOD_{SP} and AOD_t (AOD_a) observations. The fourth case, the most complicated, allowed
357 both criteria to be applied; the minimum in distance and time. No differences in the amount of
358 coincident data were found when testing whether the order in which the two criteria were applied
359 had any impact.

360 Another approach, the most commonly used for comparison (Bennouna et al., 2011; Sayer
361 et al., 2014), involves the average of all the AOD_{SP} values in the interval of ± 30 minutes compared
362 to MODIS instrument overpass time (note that AOD_t and AOD_a averages are really the daily values
363 of MODIS) located in a radius of 25 km around the sun photometer. At least two single AOD_{SP}
364 and two single AOD_t (AOD_a) observations were required to calculate the spatio-temporal average.
365 We applied a similar approach to calculate collocated daily means AE_{SP}, AE_t and AE_a. The
366 procedures described above generated a series of collocated daily means of AOD_{SP} versus AOD_t
367 (AOD_a) and AE_{SP} vs. AE_t (AE_a). Hence, by combining the former generated series of AOD (AE)
368 for Terra and Aqua we produced the coincident (Terra + Aqua) dataset. The term *collocated daily*
369 *mean AOD* will be used hereinafter although it should be stressed that this approach reduces the
370 number of observations generated by virtually a third.

371 After explaining the coincidence criteria adopted here, it is well known that this type of
372 comparison shows major differences depending on the spatial and or temporal resolution taken for
373 the MODIS sensor in relation to the ground-based instruments used (Santese et al., 2007; Levy et
374 al., 2009; Bennouna et al., 2011, 2013). The justification for using a “single observations” dataset

375 and a “collocated daily means” dataset separately to analyze this comparison is based on: a) the
376 characteristics of the surface area under study, with nearby areas of water and land; b) the
377 difference concerning how cloud cover affects data during the overpass time of the Terra and Aqua
378 platforms; and c) the possibility of including the largest amount of data; d) the fact that only single
379 observations can be compared in the case of BAOD pyrheliometer measurements.

380 **2.5 Statistics**

381 The statistics used in the present study are those commonly used (e.g., Sayer et al., 2014).
382 These are the root mean square error (RMSE), mean absolute error (MAE), median bias (BIAS),
383 the Pearson linear correlation coefficient (R), the number of coincident MODIS and sun
384 photometer cases (Cases) and the fraction (f) of the MODIS/AERONET AOD retrievals in
385 agreement within the expected uncertainty. Expected uncertainty, defined as a one standard
386 deviation confidence interval entails the sum of the absolute and relative AOD errors. Usually
387 referred to as “expected error, EE”, it was applied in accordance with equation 3 (Sayer et al.,
388 2014)

$$389 \quad EE_{DT} = \pm(0.05 + 0.15 AOD) \quad (3)$$

390 The aim is to compare the performance of the DB and DT algorithms directly (Sayer et al.,
391 2014). All of these statistical indicators were evaluated for the whole set of collocated AOD_t,
392 AOD_a, AOD_{ta} with AOD_{SP}, and BAOD; AE_t, AE_a, AE_{ta} with AE_{SP}; as well as time frequencies
393 (Figure 2) and histograms of these quantities. We also evaluated these statistics on a monthly scale
394 for the AOD values.

395

396 **3. Results and Discussion.**

397 This section is divided into four subsections. In the first subsection, we analyze in detail
398 the main results from comparing the AOD satellite MODIS sensors and the sun photometer data
399 given by the statistical indicators and linear correlations, as a result of taking two different criteria,
400 two different retrieval AOD aerosol algorithms both for the Terra and Aqua platforms. Section 3.2
401 analyzes the same type of results but under the perspective of monthly values since they represent
402 the climatology of AOD and the associated uncertainties. Section 3.3 shows AE behavior and
403 Section 3.4 analyzes the comparison of satellite MODIS data in relation to broadband aerosol
404 optical depth from solar radiation.

405 ***3.1 Comparison of AOD retrievals from sun photometer and MODIS satellite instruments.***

406 As explained, we selected MODIS AOD_t (AOD_a) and sun photometer AOD_{SP} data based
407 on two different criteria for their comparison. Results are shown in Tables 4 and 5, corresponding
408 to collocated daily means and single observations, respectively. The values of all the statistics of
409 these two tables are extraordinarily similar, with analogous behavior for the different algorithm
410 and platforms. In truth, no substantial differences are found. It must be noted that Table 4 for
411 collocated daily means contains a third less data than Table 5 based on single observations. In
412 contrast, however, the latter data have a higher associated error than daily mean data. This result
413 cannot be foreseen a priori but clearly demonstrates that either criterion may be taken, since the
414 result is basically the same.

415 Taking Table 5 together with Figure 3 of collocated daily mean values, we then analyze
416 the different behavior of the two algorithms for the Terra and Aqua platforms, when AOD_t (AOD_a)
417 from satellite are compared with the sun photometer, AOD_{SP} . Figure 3 shows the density plots of
418 the collocated daily mean AOD values from the sun photometer versus those of MODIS
419 instruments for Terra, Aqua and combined, for DB (top plots) and DT (bottom plots) algorithms.

420 The least squares linear fit lines and equations are also shown in the figure while the correlation
421 coefficients (R values) are in Table 5. In general, the plots show that low loading aerosols
422 predominate and that scatter increases for higher aerosol loadings, with a slight overestimation of
423 AOD_t (AOD_a) satellite data compared to AOD_{SP} . In all cases, the slopes are between 1 and 0.9 and
424 the intercepts are in the order of 10^{-2} (with lower values for the DT algorithm), showing very good
425 values of these parameters for Terra and Aqua for both the DT and DB algorithms.

426 Figure 3 shows that the DT algorithm displays generally better behavior than the DB
427 algorithm. The DT algorithm evidences more unified behavior as can be seen for the slope values
428 (0.96 for both Aqua and Terra) while DB changes, giving a value above 1 (1.069) for Terra and
429 below 1 for Aqua (0.901). However, these differences are not very relevant since both algorithms
430 give almost identical R values, and the difference appears for the platforms, with higher values for
431 Aqua than for Terra (~0.78 and ~0.73, respectively). A compensation effect can be observed when
432 data are combined, since in this case the slope of the DB algorithm is closer to 1 than the DT
433 algorithm, although the intercept is higher (closer to 0 for DT algorithm). For combined data, the
434 two algorithms show a more similar behavior than for separate Aqua or Terra results. Analyzing
435 Table 5, the magnitudes of the RMSE, MAE, BIAS and f statistics are lower for the DT than for
436 the DB algorithm (see the higher values of DB for Terra, column 1, and the more similar values in
437 the other columns). As mentioned, the values of these four parameters show that the DT algorithm
438 presents a more unified behavior for both platforms than the DB, which has similar values for
439 Aqua but which change significantly for Terra.

440 Although the statistical numbers in the comparison depend on the area under study,
441 comparisons between areas are always possible. A recent validation of MODIS Collection 6 AOD_a
442 (Aqua), derived using the DB algorithm, with AOD_{SP} from six AERONET stations in

443 Central/South America (CSA) and seven in Eastern North America (ENA) was reported by Sayer
444 et al. (2013). The number of pairs of collocated MODIS and AERONET daily averaged
445 observations for CSA (ENA) was 3,032 (4155). Sun photometer data were averaged within the 30
446 minute MODIS overpass time and MODIS data were averaged in the 25 km radius around the sun
447 photometer site, which makes the comparison appropriate. We selected the BIAS and R statistics
448 in Table 1, which were defined as in the present study (Sayer et al., 2013).

449 We compare those statistics with the ones given in Tables 4 and 5, calculated for
450 Camagüey. The BIAS for the CSA (ENA) stations is -0.016 (0.0094), although those of Camagüey
451 for both single observations and collocated daily means are (-0.027 and -0.033), thus showing
452 higher values for Camagüey and similar signs for CSA and the opposite for ENA. R values for
453 Camagüey for single observations and collocated daily means are 0.82 and 0.79, respectively,
454 lower by around 10 % (5 %) than the R values of 0.96 (0.86) for the CSA (ENA). However, it
455 should be noted that the number of cases used for the statistics at Camagüey was 419 for single
456 observation and 169 for collocated daily means, representing 6 % and 14 % of the 3,032 cases
457 used in the cited study. In addition, none of the stations in the CSA (ENA) regions were located in
458 the Caribbean, but south and north (Sayer, 2018). Despite the significant difference in the amount
459 of cases used in both studies and the location of the six stations, results show reasonable agreement.

460 *3.2 Monthly means values and statistics*

461 Given the close similarity in the results from single observations and collocated daily
462 means data, it seems reasonable to evaluate monthly mean values based on only one of them, i.e.,
463 for the collocated daily means data. Figure 4 shows the monthly means (based on the mean of each
464 month for every year of the measured period) and the statistics resulting from the comparison
465 between AOD_{SP} and AOD_{ta} for both the DB and DT algorithms. Tables S1 and S2 (see

466 supplementary material) also illustrate this comparison although they add separate information for
467 Terra and Aqua (see supplementary material). In Figure 4a, the multiannual monthly means from
468 the combined AOD_{ta} and AOD_{SP} for both the MODIS DB and DT algorithm are shown, providing
469 an initial overview of aerosol AOD climatology in Camaguey. It can also be seen that the DT
470 algorithm gives the best match with monthly mean AOD_{SP}.

471 The monthly RMSE and MAE plots in Figures 4b and 4c generally show increases, with
472 the increase in the AOD_{ta} for the DT algorithm and also for the DB algorithm, the exception being
473 the minimum in April for the DT algorithm (this means greater differences between satellite and
474 sunphotometer in summer than in winter). These results are consistent with the fact that AOD
475 uncertainty depends on the AOD itself (see eq. 3) and greater AOD variability in summer. The
476 AOD_{ta} peaks for the DT algorithm in March in both RMSE and MAE are also present in the results
477 for AOD_t and AOD_a, separately, and the amount of cases available for the statistics is among the
478 highest of all the months seen in Tables S1 and S2 (see supplementary material). In Table S2, for
479 the DT algorithm, we can see that the number of cases of AOD_{ta} from March to April drops by 55
480 %. However, something similar happens for the DB algorithm in Table S1, with the number of
481 AOD_{ta} cases falling from March to April by 61 %. Sampling cannot therefore be seen as the cause
482 of the RMSE and MAE peaks for the DT algorithm. We plan to revisit this feature in future studies.
483 In summer, RMSE and MAE show their maximum values associated to the maximum values of
484 the AOD resulting from Saharan dust reaching Cuba from across the Atlantic. The BIAS is
485 negative in summer for both Terra and Aqua AOD, showing that AOD_t and AOD_a observations
486 have higher magnitudes than AOD_{SP}.

487 Tabulated results of the comparison between AOD_t, AOD_a and AOD_{ta} with AOD_{SP} on a
488 monthly scale also show better results for the DB (see Table S1) than for the DT (Table S2)

489 algorithm. Here, we only discuss the results of the joint AOD_{ta} dataset using both the DT and DB
490 algorithms. In Figures 4d, the BIAS for the DT algorithm is positive from December to May, a
491 period of the year with predominant lower AOD_{ta} and AOD_{SP} values. During this period, AOD_{ta}
492 underestimates AOD_{SP} . BIAS then becomes negative from June to November, which is when
493 Saharan dust reaches the Caribbean basins. At the same time, the BIAS of the AOD_{ta} derived with
494 the DB algorithm is negative for the whole year, with higher absolute values than those from the
495 DT algorithm.

496 The correlation coefficient, R , in Figure 4e is the statistic which shows almost the same
497 agreement for the DB and DT algorithm. However, the DT shows a higher number of R -values
498 bearing higher magnitudes. R magnitudes remain over 0.5 almost the whole year round except in
499 December and January when lower AOD values occur.

500 Figure 4f shows the fraction of the AOD_{ta} (f), in agreement with AOD_{SP} within the expected
501 uncertainty, showing its higher values over 80 % from November to January, in general for both
502 algorithms. This is the period of the year with the lowest monthly mean values of both AOD_{ta} and
503 AOD_{SP} . During the rest of the year, including the period of the Saharan dust arrivals, it shows its
504 lowest values between 60 % and 75 % for the DT algorithm while values for DB below 50 % occur
505 in four of the months between June and October. The discontinuous blue line at $f = 68$ % denotes
506 a one standard deviation confidence interval, selected to describe EE. The f values above that value
507 mean the algorithm works better than expected. All the statistics demonstrate that the DT algorithm
508 performs better than the DB for the region of study. However, the lowest R values for those months
509 with the highest f values would seem to be contradictory. At present, we have no explanation for
510 this.

511 ***3.3 Comparison of Ångström Exponent by sun photometer and MODIS satellite instruments:***

512 Figure 5 shows the frequency distribution of the coincident AE_{SP} with both AE_t and AE_a
513 using the DB algorithm, as explained. As can be seen in the literature, the Ångström Exponent
514 varies between 0 and 2. Our Ångström Exponent data obtained from the AERONET sun
515 photometer measurements are within this range with a wide and smooth frequency distribution of
516 values and with a not well-defined maximum in the range 1.2 and 1.6. Neither AE_t nor AE_a present
517 any real distribution shape because there are practically no values below 1, with most being around
518 $AE = 1.5$, followed by a second maximum at $AE = 1.8$. The first, 1.5, is a regional default value
519 for AE_t and AE_a (Hsu et al., 2013; Sayer et al., 2013) assumed by the DB algorithm in the case of
520 low AOD values (AOD_t or $AOD_a < 0.2$). The second is associated with the fact that the AE_t and
521 AE_a values allowed by the aerosol optical models in Collection 6 are constrained between 0 and
522 1.8 to avoid unrealistic values (Sayer et al., 2013).

523 Table 6 shows the results of the comparison of coincident AE_t , AE_a and AE_{ta} with E_{SP} . For
524 both single observations and collocated daily mean data the statistics were calculated for the two
525 options: the first including all values and the second excluding cases with $AE = 1.5$ and 1.8. The
526 statistics in Table 6 for all values present similar values considering those derived by single
527 observation or for collocated daily mean values as expected once we know the results for AOD,
528 although similar values also appear for Terra and Aqua (no clear distinction appears between Terra
529 and Aqua). These statistics present very high values if compared with those shown for AOD.
530 Obviously, the R correlation coefficient presents very low values, which are below 0.5 (the poor
531 correlation is observed in the scatter plots similar to those in Figure 6, not shown here). Excluding
532 AE_t and AE_a values equal to 1.5 or 1.8 entails no substantial difference, only lower BIAS values.
533 Overall, the results of the comparison showed the low quantitative skill of the AE_t and AE_a for this
534 site. One factor contributing to this result is that the AE from the MODIS DB algorithm displays

535 great uncertainty for low-AOD conditions, since AE is obtained as a gradient between two small
536 AOD numbers (Wagner and Silva, 2008).

537 *3.4 Comparison of AOD between MODIS products and BAOD for the four Cuban* 538 *actinometrical stations.*

539 Two main facts limit the number of available BAOD values coincident in time with AOD_t
540 and AOD_a: the hourly time step between manual DNI observations and the required condition of
541 a clear line of sight between the pyrheliometer and a region of 5° around the Sun. Consequently,
542 only one BAOD measurement could coincide each day with AOD_t, and another with AOD_a given
543 the time coincidence criteria. Table 7 lists the number of coincident AOD_t, AOD_a, AOD_{ta}
544 observations in space and time with BAOD both for the DB and DT algorithms for each of the
545 actinometrical stations. Since the amount of coincident observations at each station is low, we
546 decided to combine all the pairs of AOD_t, AOD_a and AOD_{ta} coincident with BAOD in the four
547 sites together in order to conduct the comparison. In addition, we did not consider the very few
548 cases with values of BAOD > 0.6, around 1 % of all cases, so as to avoid the possibility of
549 inadvertent cloud contamination.

550 Table 8 contains almost the same statistics used in previous comparison satellite-sun
551 photometer data (see Table 4 and 5), both for the DB and for DT algorithms for the four
552 actinometrical stations together. The only statistic not included in Table 8 is f, the fraction of the
553 MODIS/AERONET AOD retrievals in agreement within the expected uncertainty, because such
554 uncertainty still has to be established for BAOD. We highlighted the best performing algorithm in
555 bold for each of the statistics. The AOD_a derived with the DB algorithm performs better than the
556 other three combinations of AOD_t, AOD_a, for DT and DB in accordance with all four statistics,
557 except for BIAS, where the best performing is still the DB algorithm, but for AOD_t. However, in

558 general and taking into account the low number of data and the fact that we have single
559 observations, the RMSE, MAE and BIAS for AOD_t , AOD_a , AOD_{ta} derived with both DB and DT
560 algorithms remain in the same order of magnitude as earlier Tables 4 and 5, with the exception of
561 the low values of the correlation coefficient R. The BIAS shows almost similar behavior except
562 for its best performing value. This different behavior of algorithms and platforms with respect to
563 the earlier results of Table 4-5 is clearly shown by Figure 6 where the scatter plots of the BAOD
564 vs. AOD_t , AOD_a , and AOD_{ta} are depicted. What is clear is the poor correlation given by the very
565 low values of the slope with respect to the value 1 and also the relatively high values of the intercept
566 in relation to 0, and hence the resulting low values of the R coefficient. BAOD shows a high
567 uncertainty for low values of AOD (below 2, see this range over the X axis in the plots) which are
568 those prevalent in this area (1).

569

570 **4. Conclusions**

571 This study addresses the comparisons of different sources of AOD and AE from ground-
572 based sun photometer (AERONET level 2.0 data), MODIS instruments (Terra, Aqua, and Terra +
573 Aqua) and retrievals from direct normal solar irradiance observations in Cuba.

574 The comparison of spatial and temporal coincident single observations and collocated daily
575 means of AOD_t , AOD_a , AOD_{ta} vs. AOD_{SP} shows, in general, a better performance for the Dark
576 Target (DT) than for the Deep Blue (DB) algorithm for Camagüey. In particular we found: 1)
577 small differences were found between AOD_t and AOD_a , thus justifying the combination of these
578 observations in a single dataset for climatological studies; 2) Both DT and DB algorithms are
579 better than expected (f around 80%) between November and January, but in other months
580 f is on the order of one standard deviation (f = 68%) for DT and significantly lower for DB;

581 **3) from linear correlation analysis, MODIS slightly overestimates AOD compared to the sun**
582 **photometers; 4) data from both MODIS instruments are well correlated with AERONET**
583 **AOD with regression slopes close to 1, with the DT algorithm outperforming the DB**
584 **algorithm; In addition, the comparison of multi-annual monthly means of AOD_{ta} with**
585 **AOD_{sp} indicate better agreement with results from the DT algorithm (compared to DB),**
586 **consistent with the findings above.**

587 The Ångström exponents AE_t , AE_a and AE_{ta} do not show good agreement with the spatial
588 and temporal coincident AE_{SP} values when the default-1.5 and the **constrained**-1.8 values are or
589 are not considered. Those results corroborate the **limited skills** of the MODIS derived AE, **as**
590 **indicated in previous studies.**

591 In the comparison of BAOD vs. AOD_t , AOD_a , AOD_{ta} , **where only individual**
592 **observations can be compared, the statistics indicate larger uncertainties but** of the same order
593 of magnitude as the statistics of MODIS-photometer. **Although correlations are very poor, these**
594 **results support** the potential of BAOD as a reliable source of aerosol information for
595 climatological studies in areas that lack a sun photometer or any other surface **aerosol**
596 measurement.

597

598 **5. Acknowledgements:**

599 This work has been supported by the Cuban National Program “Meteorology and
600 sustainable development for Cuba” research grant P211LH007-20 and by the Joint Agreement
601 between the University of Valladolid, Spain, and the Cuban Meteorological Institute for aerosol
602 research. JCAM wishes to thank Dr. Loraine Remer and Dr. Andrew Sayer for their contributions
603 to understanding MODIS algorithms. This research has received funding from the European

604 Union's Horizon 2020 Research and Innovation Program under grant agreement No 654109
605 (ACTRIS-2). We acknowledge the funding provided by MINECO (CTM2015-66742-R) and by
606 the Junta de Castilla y León (VA100U14).

607

608 **6. References:**

- 609 Antuña, J. C., Fonte, A., Estevan, R., Barja, B., Acea, R., Antuña Jr.: J.C., Solar radiation data
610 rescue at Camagüey, Cuba, *Bull. Am. Meteorol. Soc.*, **89**, 1507–1511.
611 <http://dx.doi.org/10.1175/2008BAMS2368.1>, 2008.
- 612 Antuña J. C., Hernández, C., Estevan, R., Barja, B., Fonte, A., Hernández, T., Antuña Jr, J. C.:
613 Camagüey’s solar radiation rescued dataset: preliminary applications, *Óptica Pura y*
614 *Aplicada*, **44** (1), 43-48, 2011.
- 615 Antuña, J. C., Estevan, R., Barja, B.: Demonstrating the Potential for First-Class Research in
616 Underdeveloped Countries: Research on Stratospheric Aerosols and Cirrus Clouds Optical
617 Properties, and Radiative Effects in Cuba (1988–2010), *Bull. Amer. Meteor. Soc.*, **93**,
618 1017–1027. <http://dx.doi.org/10.1175/BAMS-D-11-00149.1>, 2012.
- 619 Antuña-Marrero, J. C., De Frutos Baraja, A., Estevan Arredondo, R.: Joint aerosol research
620 between Cuba and Spain proves fruitful, *EOS*, **97**, doi:10.1029/2016EO060125, 2016.
- 621 Barja, B., Rosas, J., Estevan, R.: Caracterización del contenido integral del vapor de agua
622 atmosférico sobre Cuba obtenido mediante mediciones y modelación, Scientific Report,
623 Grant 200.04070, 77 pp. (In Spanish, unpublished), 2015.
- 624 Bennouna, Y. S., Cachorro, V. E., B., Toledano, C., Berjon, Prats, N., D Fuertes, González, R.;
625 Rodrigo, R., Torres, B., and De Frutos, A. M.: Comparison of atmospheric aerosol
626 climatologies over southwestern Spain derived from AERONET and MODIS. *Remote*
627 *Sens. Environ.* 115, 1272-1284, 2011, doi:10.1016/j.rse.2011.01.011.
- 628 Bennouna, Y. S., Cachorro, V. E., Torres, B., Toledano, C., Berjon, A., de Frutos, A. M. and
629 Alonso Fernandez-Coppel, I.: Atmospheric turbidity determined by the annual cycle of the

630 aerosol optical depth over north-center Spain from ground (AERONET) and satellite
631 (MODIS). *Atmos. Environ.* **67**, 353-364, 2013. doi:10.016./j.atmosenv.2012.10.065.

632 Denjean, C., Formenti, P., Desboeufs, K., Chevaillier, S., Triquet, S., Maillé, M., Cazaunau, M.,
633 Laurent, B., Mayol-Bracero, O.L. :, Vallejo, P., Quiñones, M., Gutierrez-Molina, I. E.,
634 Cassola, F., Prati, P., and Andrews, E., and Ogren, J. : Size distribution and optical
635 properties of Africanm mineral dust after intercontinental transport, *J. Geophys. Res.*, **121**,
636 7117–7138, doi:10.1002/2016JD024783. 2016.

637 Eck, T., Holben, B., Reid, J. Dubovik, O.: Wavelength dependence of the optical depth of biomass
638 burning, urban, and desert dust aerosols. *J. Geophys. Res.*, **104**, 31333_31349, 1999.

639 Estevan, R.: Certificación de depósito legal facultativo de obras protegidas; software: “Actino
640 2.0”; CENDA 218-2010. *(In Spanish)*, 2010.

641 Estevan R., Antuña, J.C., Barja, B., Hernández, C.E., Hernández, T., García, F., Rosas, J., Platero,
642 I. Y.: Climatología de la Radiación solar en Camagüey 1981 – 2010, *Scientific Report*,
643 Grant 01301216, 41 pp. *(In Spanish, unpublished)*, 2016.

644 Fonte, A., Antuña, J.C.: Caracterización del espesor óptico de banda ancha de los aerosoles
645 troposféricos en Camagüey, Cuba, *Revista Cubana de Meteorología*, **17**, No. 1, pp. 15-26,
646 2011.

647 García, F., Estevan, R., Antuña-Marrero, J. C., Rosas, J., Platero, I. Y., Antuña-Sánchez, J., C.
648 Díaz, N.: Determinación de la Línea Base del Espesor Óptico de Aerosoles de Banda Ancha
649 y comparación con datos de fotómetro solar. *Óptica Pura y Aplicada*, **48**(4), 249-258.doi:
650 10.7149/OPA.48.4.249, 2015.

651 GGO: Manual for the setup and operation of solar radiation instruments. Ed. Guidrometeoizdat,
652 124 pp. *(In Russian)*, 1957.

653 Gkikas, A., Hatzianastassiou, N., Mihalopoulos, N., Katsoulis, V., Kazadzis, S., Pey, J., Querol,
654 X., and Torres, O.: The regime of intense desert dust episodes in the Mediterranean based on
655 contemporary satellite observations and ground measurements, *Atmos. Chem. Phys.*, *13*(23),
656 12135-12154, doi:10.5194/acp-13-12135-2013, 2013.

657 Gkikas, A., Basart, S., Hatzianastassiou, N., Marinou, E., Amiridis, V., Kazadzis, S., Pey, J.,
658 Querol, X., Jorba, O., Gassó, S., and Baldasano, J. M.: Mediterranean desert dust outbreaks
659 and their vertical structure based on remote sensing data, *Atmos. Chem. Phys. Discuss.*, *15*,
660 27675-27748, doi:10.5194/acpd-15-27675-2015, 2015.

661 GOAC: Manual de Observaciones Actinométricas, 37 pp. (*In Spanish, unpublished*), 2010.

662 Gueymard, C.A.: Turbidity determination from broadband irradiance observations: A detailed
663 multicoefficient approach. *J. Appl. Meteorol.* **37**: 414-435, 1998.

664 Gueymard, C. A.: Aerosol turbidity derivation from broadband irradiance observations:
665 Methodological advances and uncertainty analysis. *Solar 2013 Conf.*, Baltimore, MD,
666 American Solar Energy Soc., 8 pp., 2013.

667 Holben, B. N., Tanré, D., Smirnov, A., Eck, T. F., Slutsker, I., Abuhassan, N., Newcomb, W. W.,
668 Schafer, J., Chatenet, B., Lavenue, F., Kaufman, Y. J., Castle, J. V., Setzer, A., Markham,
669 B., Clark, D., Frouin, R., Halthore, R., Karnieli, A., O'Neill, N. T., Pietras, C., Pinker, R.
670 T., Voss, K., Zibordi, G.: An emerging ground-based aerosol climatology: Aerosol optical
671 depth from AERONET, *J. Geophys. Res.*, **106**, 12,067–12,097, 2001.

672 Hsu, N. C., Tsay, S. C., King, M. D., Herman, J. R.: Aerosol Properties Over Bright-Reflecting
673 Source Regions, *IEEE T. Geosci. Remote*, **42**, 557–569, doi:10.1109/TGRS.2004.824067,
674 2004.

675 Hsu, N. C., Tsay, S. C., King, M. D., Herman, J. R.: Deep blue retrievals of Asian aerosol
676 properties during ACE-Asia, *IEEE T. Geosci. Remote*, **44**, 3180–3195,
677 doi:10.1109/TGRS.2006.879540, 2006.

678 Hsu, N. C., Jeong, M.-J., Bettenhausen, C., Sayer, A. M., Hansell, R., Seftor, C. S., Huang, J.,
679 Tsay, S.-C.: Enhanced Deep Blue aerosol retrieval algorithm: the second generation, *J.*
680 *Geophys. Res.*, **118**, 9296–9315, doi:10.1002/jgrd.50712, 2013.

681 IPCC: Climate Change 2013. The Physical Science Basis –Contribution of Working Group I to
682 the Fifth Assessment Report of the Intergovernmental Panel on Climate Change, Stocker
683 TF, Qin D, Plattner G-K, Tignor M, Allen SK, Boschung J, Nauels A, Xia Y, Bex V,
684 Midgley PM. (eds). Cambridge University Press: Cambridge, UK and New York, NY,
685 2013.

686 Kahn, R. A., M. J. Garay, D. L. Nelson, R. C. Levy, M. A. Bull, D. J. Diner, J. V. Martonchik, E.
687 G. Hansen, L. A. Remer, and D. Tanré, Response to “Toward unified satellite climatology
688 of aerosol properties: 3. MODIS versus MISR versus AERONET”, *J. Quant. Spectrosc.*
689 *Radiat. Transfer*, **112**(5), 901–909, doi:10.1016/j.jqsrt.2010.11.001, 2011.

690 Kaufman, Y. J., Wald, A. E., Remer, L. A., Gao, B.-C., Li, R.-R. and Flynn, L.: The MODIS 2.1-
691 μm channel-correlation with visible reflectance for use in remote sensing of aerosol, *IEEE*
692 *T. Geosci. Remote*, **35**, 1286–1298, doi:10.1109/36.628795, 1997a.

693 Kaufman, Y. J., Tanré, D., Remer, L. A., Vermote, E. F., Chu, A., Holben, B. N.: Operational
694 remote sensing of tropospheric aerosol over land from EOS moderate resolution imaging
695 spectroradiometer, *J. Geophys. Res.*, **102**, 17051–17068, doi:10.1029/96JD03988, 1997b.

696 Kaufman, Y. J., Koren, I., Remer, L., Tanré, D., Ginoux, P., and Fan, S.: Dust transport and
697 deposition observed from the Terra-Moderate Resolution Imaging Spectroradiometer
698 (MODIS) spacecraft over the Atlantic Ocean. *J. Geophys. Res. Atmos.*, **110**, D10S12, 2005.

699 Kirilov, T. B., Vlasov, Yu. B., Flaum, M. Ya.: Manual para la operación e instalación de
700 instrumentos de radiación solar, Ed.Guidrometeoizdat, Leningrad, 124 pp. (In Russian),
701 1957.

702 Knippertz, P., Stuut, J.-B.W., 2014. Chapter 1 Introduction. In: Knippertz, P., Stuut, J.-B.W.
703 (Eds.), Mineral Dust: A Key Player in the Earth System. Springer, New York, pp. 1–14,
704 <http://dx.doi.org/10.1007/978-94-017-8978-3>, 2014.

705 Levy, R. C., Remer, L., Mattoo, S., Vermote, E., and Kaufman, Y.: Second-generation operational
706 algorithm: Retrieval of aerosol properties over land from inversion of moderate resolution
707 imaging spectroradiometer spectral reflectance. *J. Geophys. Res. Atmos.*, **112**, D13211,
708 2007.

709 Levy, R. C., Leptoukh, G., Kahn, R., Zubko, V., Gopalan, A., and Remer, L.: A critical look at
710 deriving monthly aerosol optical depth from satellite data. *IEEE Transactions on*
711 *Geoscience and Remote Sensing*, **47**(8), 2942–2956, 2009.

712 Levy, R. C., Remer, L. A., Kleidman, R. G., Mattoo, S., Ichoku, C., Kahn, R., Eck, T. F.: Global
713 evaluation of the Collection 5 MODIS dark-target aerosol products over land, *Atmos.*
714 *Chem. Phys.*, **10**, 10399-10420, doi:10.5194/acp-10-10399-2010, 2010.

715 Levy, R. C., Mattoo, S., Munchak, L. A., Remer, L. A., Sayer, A. M., Patadia, F., Hsu, N. C.: The
716 Collection 6 MODIS aerosol products over land and ocean, *Atmos. Meas. Tech.*, **6**, 2989-
717 3034, doi:10.5194/amt-6-2989-2013, 2013.

718 Levy, R. C., Munchak, L.A., Mattoo, S., Patadia, F., Remer, L.A., and Holz, R. E.: Towards a
719 long-term global aerosol optical depth record: applying a consistent aerosol retrieval
720 algorithm to MODIS and VIIRS-observed reflectance. *Atmos. Meas. Tech.*, **8**, 4083–4110,
721 2015. doi:10.5194/amt-8-4083-2015.

722 Long, C. N., Shi, Y.: The QCRad Value Added Product: Surface Radiation Measurement Quality
723 Control Testing, Including Climatology Configurable Limits, Office of Biological and
724 Environmental Research, U.S. Department of Energy, pp. 69, 2006.

725 Long, C. N., Shi, Y.: An Automated Quality Assessment and Control Algorithm for Surface
726 Radiation Observations. *The Open Atmospheric Science Journal*, **2**, 23-37, 2008.

727 Martínez, E., Campos, A., Borrajero, I., Vázquez, A.: Algunos índices de turbidez del aire en la
728 Ciudad de la Habana, *Revista Cubana de Meteorología*, **1** (1), pp. 57-60, 1988.

729 Mielonen, T., Levy, R. C., Aaltonen, V., Komppula, M., de Leeuw, G., Huttunen, J., Lihavainen,
730 H., Kolmonen, P., Lehtinen, K. E. J., Arola, A.: Evaluating the assumptions of surface
731 reflectance and aerosol type selection within the MODIS aerosol retrieval over land: the
732 problem of dust type selection, *Atmos. Meas. Tech.*, **4**, 201–214, doi:10.5194/amt-4-201-
733 2011, 2011.

734 Mishchenko M.I., Li Liu, Geogdzhayev, I. V., Travis, L. D., Cairns, B., Lacis, A. A.: Toward
735 unified satellite climatology of aerosol properties.: 3. MODIS versus MISR versus
736 AERONET, *J. Quant. Spectrosc. Radiat. Transfer*, **111**, 540-552, 2010.

737 Ohmura, A., Dutton, E., Forgan, B., Froehlich, C., Gilgen, H., Hegner, H., Heimo, A., Koenig-
738 Langlo, G., McArthur, B., Mueller, G., Philipona, R., Pinker, R., Whitlock, C., Wild, M.:
739 Baseline Surface Radiation Network (BSRN/WCRP), a new precision radiometry for
740 climate research. *Bull. Am. Meteorol. Soc.*, **79**, 2115-2136, 1998.

741 Papadimas, C.D., Hatzianastassiou, N., Mihalopoulos, N., Kanakidou, M., Katsoulis, B. D., and
742 Vardavas, I.: Assessment of the MODIS Collections C005 and C004 aerosol optical depth
743 products over the Mediterranean basin, *Atmos. Chem. Phys.*, **9**, 2987-2999;
744 doi.org/10.5194/acp-9-2987-2009, 2009.

745 Prospero, J. M., Lamb, P. J.: African droughts and dust transport to the Caribbean: Climate change
746 implications. *Science*, **302**, 1024–1027, 2003.

747 Prospero, J. M., Mayol-Bracero, O. L.: Understanding the transport and impact of African dust on
748 the Caribbean Basin, *Bull. Am. Meteorol. Soc.*, **94**(9), 1329–1335, 2013.

749 Prospero, J. M., Collard, F.-X., Molinié, J., Jeannot, A.: Characterizing the annual cycle of African
750 dust transport to the Caribbean Basin and South America and its impact on the environment
751 and air quality, *Global Biogeochem. Cycles*, **29**, 757–773, doi:10.1002/2013GB004802,
752 2014.

753 Remer, L. A., Tanré, D., Kaufman, Y. J., Ichoku, C., Mattoo, S., Levy, R., Chu, D. A., Holben, B.
754 N., Dubovik, O., Smirnov, A., Martins, J.V., Li, R. R., Ahmad, Z.: Validation of MODIS
755 aerosol retrieval over ocean. *Geophys. Res. Lett.*, 29(12), 1618, 2002.

756 Remer, L. A., Kaufman, Y. J., Tanre, D., Mattoo, S., Chu, D. A., Martins, J. V., Li, R. R., Ichoku,
757 C., Levy, R. C., Kleidman, R. G., Eck, T.F., Vermote, E., Holben, B. N.: The MODIS
758 aerosol algorithm, products, and validation". *J. Atmos. Sci.*, 62(4), 947-973, 2005.

759 Remer, L. A., Tanré, D., Kaufman, Y., Levy, R., and Mattoo, S.: Algorithm for remote sensing of
760 tropospheric aerosol from MODIS: Collection 005. [https://modis-](https://modis-images.gsfc.nasa.gov/docs/MOD04:MYD04_ATBD_C005_rev1.pdf)
761 [images.gsfc.nasa.gov/docs/MOD04:MYD04_ATBD_C005_rev1.pdf](https://modis-images.gsfc.nasa.gov/docs/MOD04:MYD04_ATBD_C005_rev1.pdf).

762 Sayer, A. M., Hsu, N. C., Bettenhausen, C., Jeong, M.-J.: Validation and uncertainty estimates for
763 MODIS Collection 6 “Deep Blue” aerosol data, *J. Geophys. Res. Atmos.*, **118**, 7864–7872,
764 doi:10.1002/jgrd.50600, 2013.

765 Sayer, A. M., Munchak, L. A., Hsu, N. C., Levy, R. C., Bettenhausen, C., Jeong, M.-J.: MODIS
766 Collection 6 aerosol products: Comparison between Aqua’s e-Deep Blue, Dark Target, and

767 “merged” data sets, and usage recommendations, *J. Geophys. Res. Atmos.*, **119**, 13,965–
768 13,989, doi:10.1002/2014JD022453, 2014.

769 Santese, M., De Tomasi, M. F. and, Perrone, M. R.: AERONET versus MODIS aerosol parameter
770 at different spatial resolutions over southeast Italy, *J. Geophys. Res.*, **112**, D10214,
771 doi:10.1029/2006JD007742, 2007.

772 Seinfeld, J. H. and S. N. Pandis.: Atmospheric chemistry and physics: from air pollution to climate
773 change. 3rd edition, John Wiley & Sons, Inc., ISBN: 9781118947401, 1120 pp., 2016.

774 Smirnov, A., Holben, B. N., Eck, T. F., Dubovik, O., Slutsker, I.: Cloud-screening and quality
775 control algorithms for the AERONET database, *Remote Sens. Environ.*, **73**(3), 337–349,
776 2000.

777 Swap, R., Garstang, M., Greco, S., Talbot, R., Kallberg, P.: Saharan dust in the Amazon basin.
778 *Tellus*, **44B**, 133–149, 1992.

779 Tanré, D., Kaufman, Y. J., Herman, M., Mattoo, S.: Remote sensing of aerosol properties over
780 oceans using the MODIS/EOS spectral radiances, *J. Geophys. Res.*, **102**, 16971–16988,
781 1997.

782 Velasco-Merino, C., Mateos, D., Toledano, C.; Prospero, J. M., Molinie, J., Euphrasie-Clotilde,
783 L., González, R., Cachorro, V. e., Calle, A., and De Frutos, A. M.: Impact of long-range
784 transport over the Atlantic Ocean on Saharan dust optical and microphysical properties.
785 *Atmos. Chem. Phys. Disc.*, <https://doi.org/10.5194/acp-2017-1089>, 2017

786 Wagner, F., and Silva A. M.: Some considerations about Ångström exponent distributions. *Atmos.*
787 *Chem. Phys.*, **8**, 481–489, 2008.

788 Witte, J. C., A.R. Douglass, A. da Silva, O. Torres, R.C. Levy, and B.N. Duncan, (2011). NASA
789 A-Train and Terra observations of the 2010 Russian wildfires, *Atmos. Chem. Phys.*, 11,
790 9287-9301, doi:10.5194/acp-11-9287-2011, 2011.

791 Yu, H. , M. Chin, T. Yuan, H. Bian, L. A. Remer, J. M. Prospero, A. Omar, D. Winker, Y. Yang,
792 Y. Zhang, Z. Zhang and C. Zhao, The fertilizing role of African dust in the Amazon
793 rainforest: A first multiyear assessment based on data from Cloud-Aerosol Lidar and
794 Infrared Pathfinder Satellite Observations, *Geophys. Res. Lett.*, **42**, 1984–1991,
795 doi:10.1002/2015GL063040, 2015.

796 Zhao, T. X.-P., Stowe, L. L., Smirnov, A., Crosby, D., Sapper, J., McClain, C. R.: Development
797 of a global validation package for satellite oceanic aerosol optical thickness retrieval based
798 on AERONET observations and its application to NOAA/NESDIS operational aerosol
799 retrievals, *J. Atmos. Sci.*, **59**, 294– 312, 2002.

800
801
802
803
804
805
806
807
808
809
810
811
812
813

814 **Tables:**

815

816 Table 1: Aerosol products from the MODIS Collection 6 dataset used in the present study

Product	Description
Deep_Blue_Aerosol_Optical_Depth_550_Land_Best_Estimate	Deep Blue AOT at 0.55 micron for land with higher quality data (Quality flag=2,3)
Deep_Blue_Angstrom_Exponent_Land	Deep Blue Angstrom Exponent for land with all quality data (Quality flag=1,2,3)
Optical_Depth_Land_And_Ocean	AOT at 0.55 micron for both ocean (Average) (Quality flag=1,2,3) and land (corrected) (Quality flag=3)

817

818

819 Table 2: Information about Cuban actinometrical stations operating under the Solar Radiation Diagnostic Service

820 (SRDS). Available number of BAOD observations included in column 6 and the period covered in the last column.

Code	Station Name	Latitude	Longitude	Height (m)	No. Obs.	Period
78355	Camagüey (CMW)	21.42	-77.85	122 m	2495	2001-2015
78330	Jovellanos (JVN)	22.80	-81.14	23 m	1182	2010-2015
78342	Topes de Collantes (TPC)	21.92	-80.02	766 m	1358	2011-2015
78321	Santa Fé (LFE)	21.73	-82.77	32 m	1756	2011-2015

821

822

823 Table 3: Number of available non-negative AOD_a, AOD_t, AE_a and AE_t data spatially coincident with the Camagüey

824 sunphotometer in a radius of 25 km for each retrieval algorithm, DB and DT for the whole period 2001-2015, as well

825 as the period 2008-2014, when sunphotometer data, AOD_{SP} and AE_{SP}, are available.

826

827

Period	2001-2015			2008-2014		
Algorithm	DB		DT	DB		DT
Parameter	AOD	AE	AOD	AOD	AE	AOD
Terra	6884	8111	6311	3418	4024	3166
Aqua	2445	3909	2869	1329	1534	2093

830

831

832

833 Table 4: Statistics of the comparison between collocated daily means of AOD_t and AOD_a with AOD_{SP} and the
 834 combined AOD_{ta} .

	AOD _{SP} vs. AOD _t		AOD _{SP} vs. AOD _a		AOD _{SP} vs. AOD _{ta}	
	DB	DT	DB	DT	DB	DT
RMSE	0.084	0.060	0.065	0.062	0.078	0.061
MAE	0.062	0.045	0.046	0.047	0.056	0.046
BIAS	-0.053	-0.001	-0.033	0.006	-0.046	0.002
R	0.730	0.729	0.785	0.779	0.741	0.753
f	0.656	0.803	0.763	0.795	0.694	0.800
Cases	311	335	169	254	480	589

835

836

837 Table 5: Statistics of the comparison between collocated single observation of AOD_t and AOD_a with AOD_{SP} and
 838 combined AOD_{ta} .

	AOD _{SP} vs. AOD _t		AOD _{SP} vs. AOD _a		AOD _{SP} vs. AOD _{ta}	
	DB	DT	DB	DT	DB	DT
RMSE	0.081	0.061	0.063	0.064	0.076	0.062
MAE	0.059	0.046	0.044	0.050	0.054	0.047
BIAS	-0.048	0.007	-0.027	0.017	-0.042	0.010
R	0.716	0.701	0.817	0.794	0.744	0.742
f	0.664	0.773	0.773	0.784	0.699	0.777
Cases	880	900	419	500	1299	1400

839

840

841 Table 6: Statistics of the comparison between AE_t, AE_a and AE_{ta} with AE_{SP} for single observations and daily mean
 842 values.

	Single observations			Single observations (Except AE 1.5 & 1.8)			Collocated daily means			Collocated daily means (Except AE 1.5 & 1.8)		
	AE _t	AE _a	AE _{ta}	AE _t	AE _a	AE _{ta}	AE _t	AE _a	AE _{ta}	AE _t	AE _a	AE _{ta}
RMSE	0.637	0.692	0.658	0.575	0.609	0.587	0.637	0.659	0.645	0.548	0.578	0.561
MAE	0.494	0.553	0.516	0.446	0.496	0.464	0.490	0.512	0.498	0.431	0.466	0.445
BIAS	-0.327	-0.337	-0.331	-0.129	-0.101	-0.119	-0.398	-0.384	-0.393	-0.189	-0.139	-0.167
R	-0.187	-0.426	-0.272	-0.191	-0.444	-0.269	-0.259	-0.414	-0.308	-0.124	-0.400	-0.236
Cases	615	374	989	353	189	542	311	169	480	172	120	292

843

844

845 Table 7: Number of coincident cases of AOD_t, AOD_a, AOD_{ta} with BAOD both for the DB and for DT algorithms.

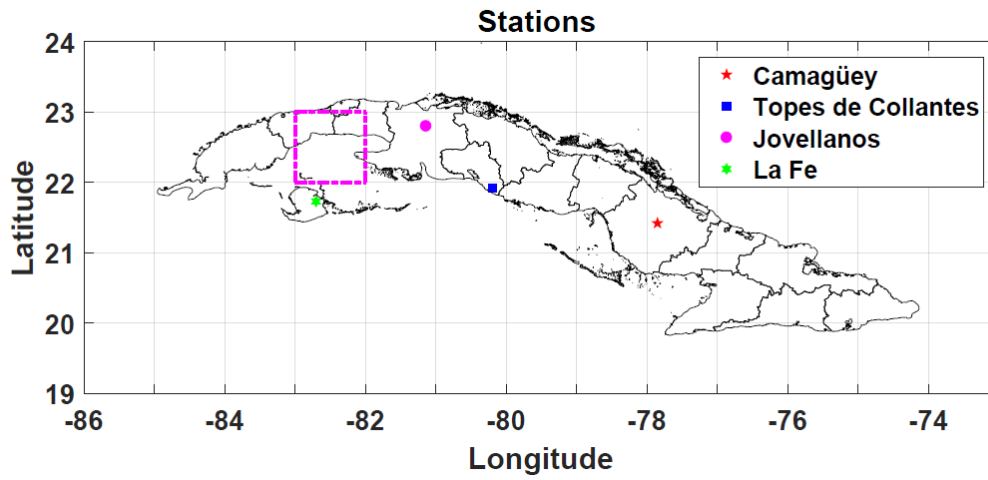
Station:	BAOD vs. AOD _t		BAOD vs. AOD _a		BAOD vs. AOD _{ta}	
	DB	DT	DB	DT	DB	DT
Camagüey	166	171	66	79	232	250
Topes de Collantes	112	138	49	76	161	214
Jovellanos	65	65	35	34	100	99
La Fe	34	66	46	85	80	151
All combined	377	440	196	274	573	714

846
 847 Table 8: Statistics of the comparison between the single observations of BAOD at the four actinometrical stations
 848 coincident in space and time with the single observation (L2) of AOD_t, AOD_a and AOD_{ta}. In bold, the values of best
 849 agreement.

Camagüey, La Fe, Topes de Collantes & Jovellanos						
	BAOD vs. AOD _t		BAOD vs. AOD _a		BAOD vs. AOD _{ta}	
	DB	DT	DB	DT	DB	DT
RMSE	0.080	0.087	0.073	0.088	0.078	0.088
MAE	0.055	0.063	0.048	0.066	0.052	0.064
BIAS	0.001	0.027	0.014	0.049	0.005	0.035
R	0.455	0.325	0.501	0.417	0.468	0.355
Cases	373	436	191	268	564	704

850
 851
 852
 853
 854
 855
 856
 857
 858
 859
 860 **Figure and Captions:**

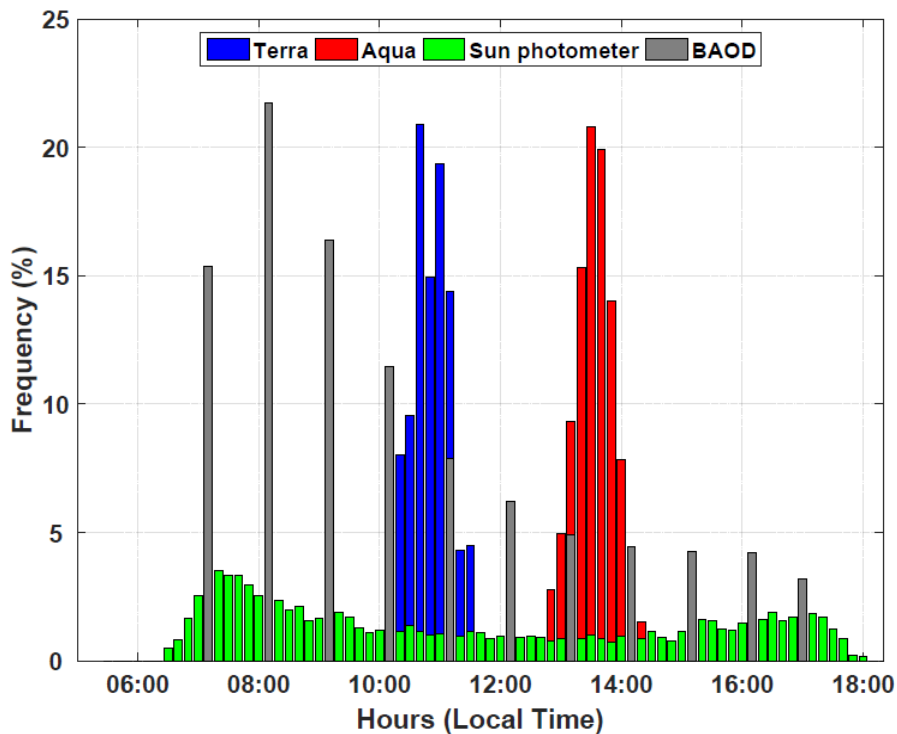
861



862

863 **Figure 1:** Map of Cuba locating the stations where the sun photometer and the four broadband
864 pyr heliometer observations are conducted.

865

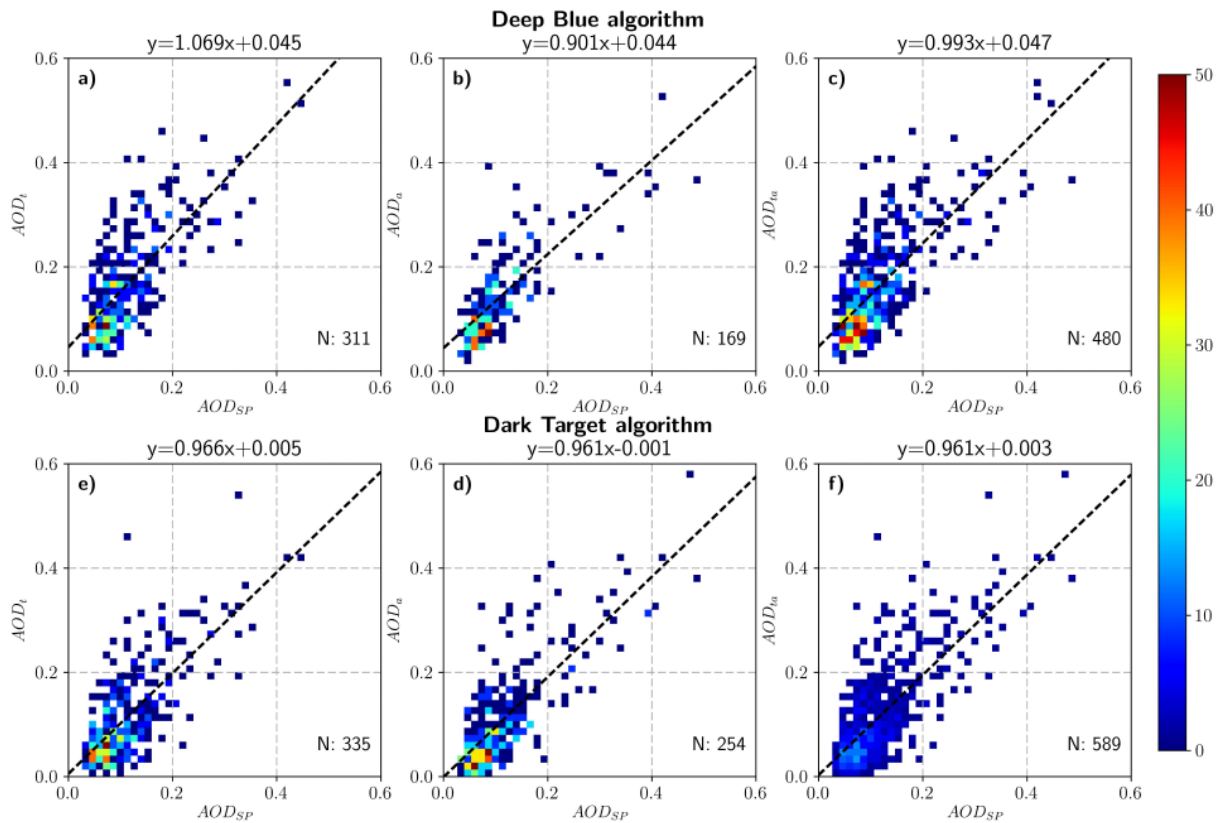


867

868 **Figure 2:** Frequencies of the time of the day (Local Time) overpass of Terra and Aqua (blue and
 869 red respectively) Camagüey’s sun photometer site in a radius of 25 km for the period
 870 2001 to 2015. In green the time frequencies for the Camagüey’s sun photometer
 871 observations in the period 2008 to 2014. In addition, the time frequencies for the direct
 872 radiation observations used to calculate the BAOD. The bar width is 10 minutes for
 873 Terra, Aqua and the sun photometer and 1 hour for the BAOD.

874

875

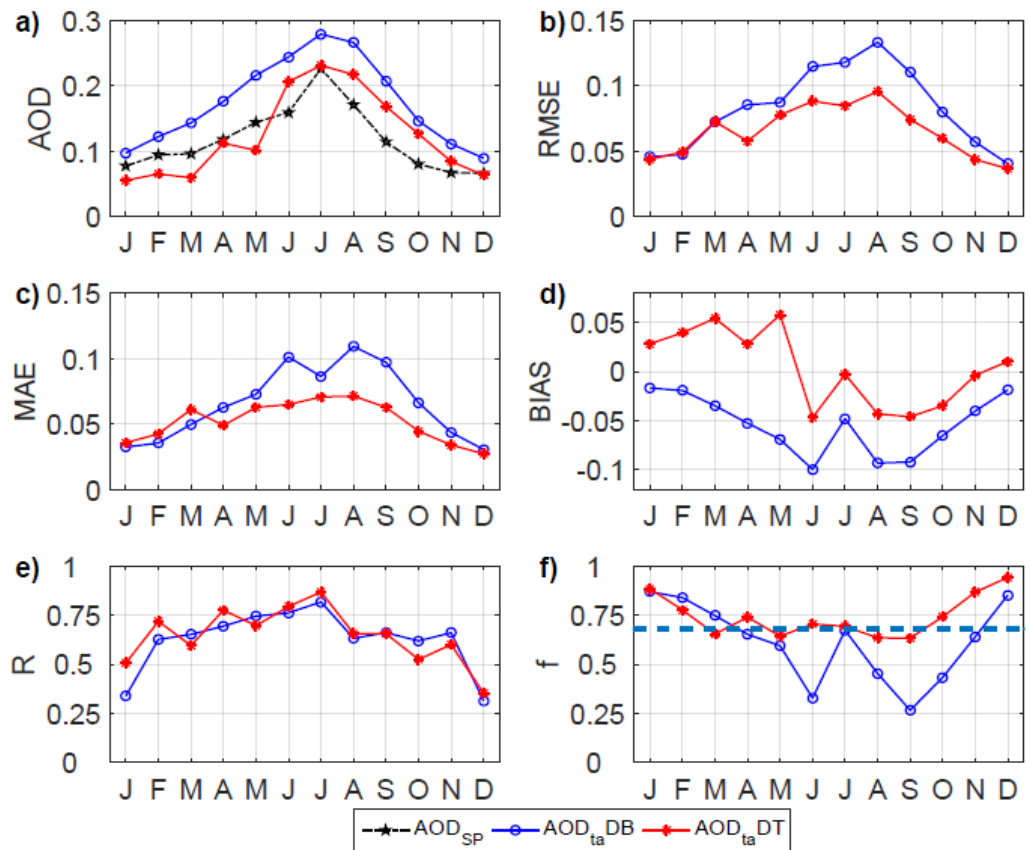


876

877 **Figure 3:** Collocated “daily mean” density scatter plots of the coincident AOD observations from
878 the sun photometer and Terra and Aqua MODIS instruments for DB and DT
879 algorithms.: a) to c) AOD_{SP} vs AOD_t , AOD_a and AOD_{ta} respectively for DB
880 algorithm; d) to f) Idem for DT algorithm. The data density is represented by the color
881 scale, showing the number of data points located in a particular area of the plot. Linear
882 regression is given by the black discontinuous line and the corresponding equation.
883 The number of data points appears in the right bottom.

884

885



887

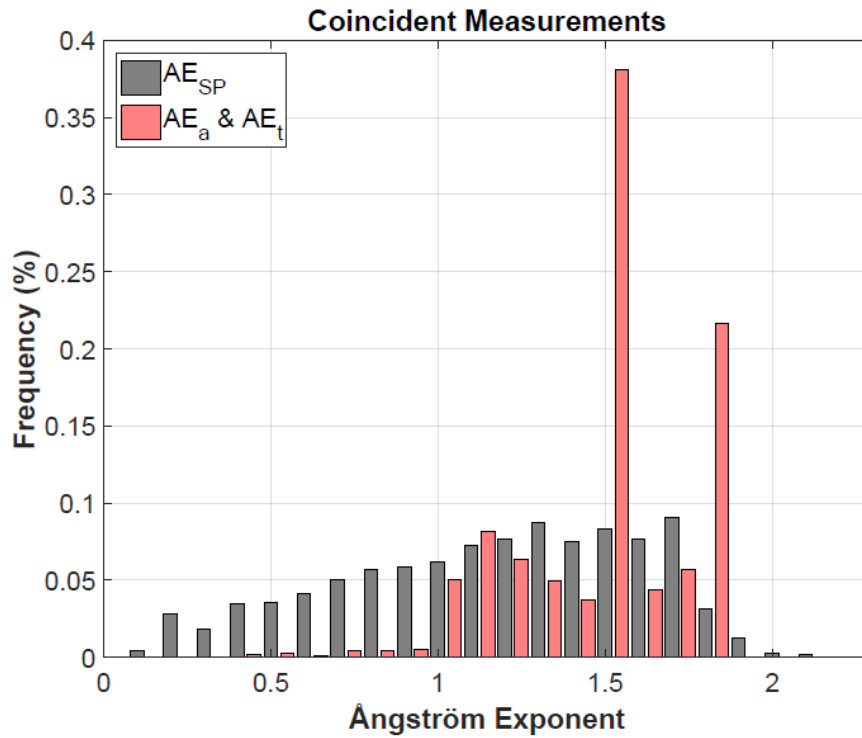
888 **Figure 4:** Monthly means and statistics (RMSE, MAE.....) resulting from the comparison
 889 between AOD_{SP} and AOD_{ta} for both DB and DT algorithms: a) Monthly means of the
 890 AOD_{SP} and AOD_{ta} for both DB and DT algorithms; b) RMSE for the comparison
 891 between AOD_{SP} and AOD_{ta} for both DB and DT algorithms; c) Idem for MAE, d) for
 892 BIAS, e) for R and f) for f. The blue discontinuous line at $f= 68 \%$ represent one
 893 standard deviation confidence interval for the EE indicator.

894

895

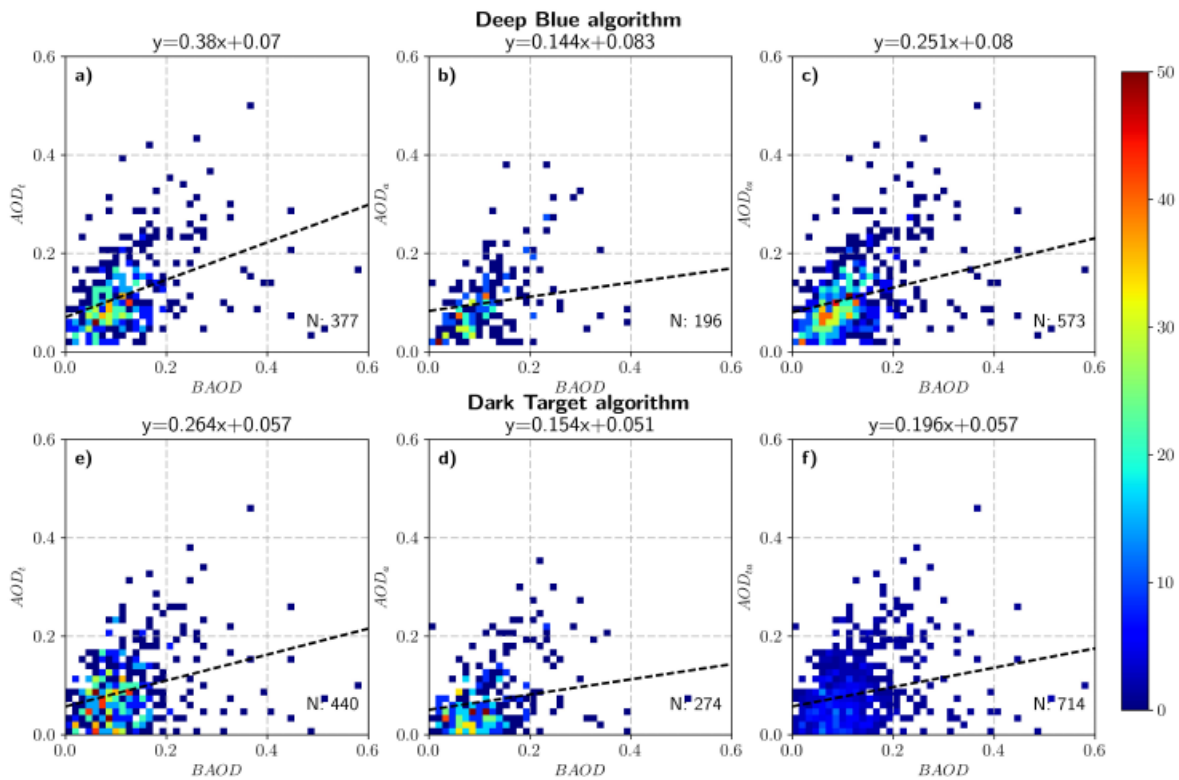
896

897



899

900 **Figure 5:** Frequency distribution of the Angstrom exponent (AE) values from both MODIS
 901 instruments Terra and Aqua and the sun photometer coincident in ± 30 minutes and 25
 902 km radius around Camagüey.
 903



905

906 **Figure 6:** Single observations density scatter plots of the coincident BAOD observations from the
 907 broadband pyrheliometer and Terra and Aqua MODIS instruments for DB and DT
 908 algorithms.: a) to c) BAOD vs. AOD_t , AOD_a and AOD_{ta} respectively for DB
 909 algorithm; d) to f) Idem for DT algorithm. The data density is represented by the color
 910 scale, showing the number of data points located in a particular area of the plot.
 911 Linear regression line is shown by the black discontinuous line and the corresponding
 912 equation. The number of data points appears in the right bottom.

913

914